Earth and Planetary Science Letters 539 (2020) 116223

Contents lists available at ScienceDirect

Earth and Planetary Science Letters

www.elsevier.com/locate/epsl

An intermediate-depth source of hydrothermal ^{3}He and dissolved iron in the North Pacific

W.J. Jenkins [a,*], M. Hatta [b], J.N. Fitzsimmons [c], R. Schlitzer [d], N.T. Lanning [c], A. Shiller [e], N.R. Buckley [f], C.R. German [a], D.E. Lott III [a], G. Weiss [b], L. Whitmore [e], K. Casciotti [g], P.J. Lam [h], G.A. Cutter [f], K.L. Cahill [a]

[a] Woods Hole Oceanographic Institution, Woods Hole, MA 02543, USA
[b] Department of Oceanography, University of Hawaii at Manoa, HI 96822, USA
[c] Department of Oceanography, Texas A & M University, College Station, TX 77843, USA
[d] Alfred Wegener Institute, 27568 Bremerhaven, Germany
[e] Center for Trace Analysis, University of Southern Mississippi, Stennis Space Center, MS 39529, USA
[f] Department of Ocean, Earth, and Atmospheric Sciences, Old Dominion University, Norfolk, VA 23529-0276, USA
[g] Department of Earth System Science, Stanford University, Stanford, CA 94305, USA
[h] Department of Ocean Sciences, University of California, Santa Cruz, Santa Cruz, CA 95064, USA

ARTICLE INFO

Article history:
Received 11 December 2019
Received in revised form 10 March 2020
Accepted 11 March 2020
Available online 30 March 2020
Editor: L. Robinson

Keywords:
submarine hydrothermal vents
seawater dissolved iron and manganese
helium isotopes
marine primary productivity
North Pacific circulation

ABSTRACT

We observed large water column anomalies in helium isotopes and trace metal concentrations above the Loihi Seamount. The ^{3}He/^{4}He of the added helium was 27.3 times the atmospheric ratio, clearly marking its origin to a primitive mantle plume. The dissolved iron to ^{3}He ratio (dFe:^{3}He) exported to surrounding waters was $9.3 \pm 0.3 \times 10^{6}$. We observed the Loihi ^{3}He and dFe "signal" at a depth of 1100 m at several stations within ~100 – 1000 km of Loihi, which exhibited a distal dFe:^{3}He ratio of $\sim 4 \times 10^{6}$, about half the proximal ratio. These ratios were remarkably similar to those observed over and near the Southern East Pacific Rise (SEPR) despite greatly contrasting geochemical and volcanic-tectonic origins. In contrast, the proximal and distal dMn:^{3}He ratios were both $\sim 1 \times 10^{6}$, less than half of that observed at the SEPR. Dissolved methane was minimally enriched in waters above Loihi Seamount and was distally absent. Using an idealized regional-scale model we replicated the historically observed regional ^{3}He distribution, requiring a hydrothermal ^{3}He source from Loihi of 10.4 ± 4.2 mol a^{-1}, ~2% of the global abyssal hydrothermal ^{3}He flux. From this we compute a corresponding dFe flux of ~40 Mmol a^{-1}. Global circulation model simulations suggest that the Loihi-influenced waters eventually upwell along the west coast of North America, also extending into the shallow northwest Pacific, making it a possibly important determinant of marine primary production in the subpolar North Pacific.

© 2020 Elsevier B.V. All rights reserved.

1. Introduction

It has long been recognized that the availability of dissolved iron is a limiting factor for oceanic biological production (Martin and Gordon, 1988). Eolian sources of this micronutrient were regarded as determining factors for global marine production on glacial-interglacial timescales (Berger and Wefer, 1991). However, the importance of hydrothermal iron has only recently been recognized (Tagliabue et al., 2010, 2017), and it has only now been quantified by the use of hydrothermal ^{3}He as a "flux gauge" (Resing et al., 2015). As part of the International GEOTRACES program, the U.S. Pacific Meridional Transect along ~152°W (GP15) was occupied during the autumn of 2018. We present here results from stations in the vicinity of the Loihi Seamount (~18.9°N, 154.2°W) showing the relationship between dissolved iron, manganese, methane, and hydrothermal ^{3}He over the seamount and distally for neighboring stations near the 1100 m injection depth. We use contemporaneous dissolved Fe, Mn, and ^{3}He measurements at nearby stations to unambiguously quantify the helium isotope-metal relationships and fluxes, and to determine their role in regional biogeochemical cycles. The location of the stations that inform this study are shown as red stars in Fig. 1, which is a chart

* Corresponding author.
E-mail address: wjenkins@whoi.edu (W.J. Jenkins).

https://doi.org/10.1016/j.epsl.2020.116223
0012-821X/© 2020 Elsevier B.V. All rights reserved.

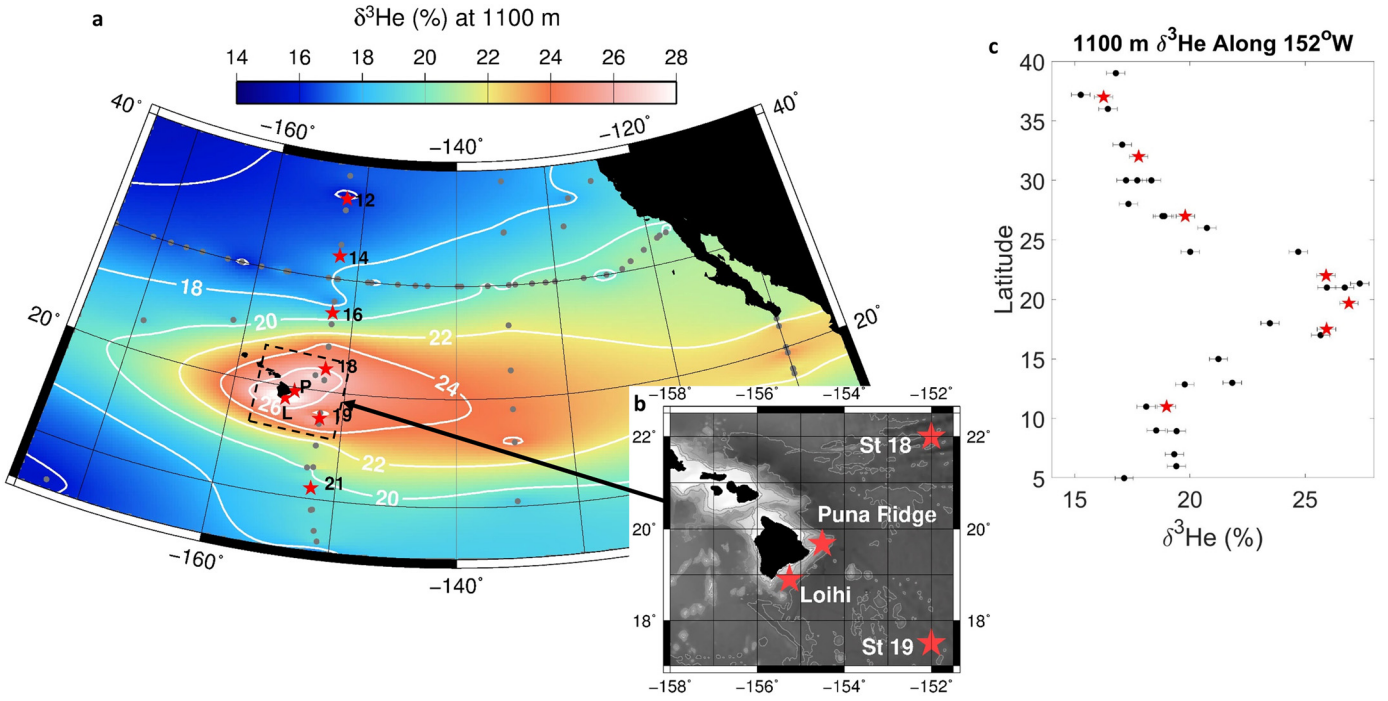

Fig. 1. ***a, Location map*** of the GEOTRACES GP15 stations (red stars, black labels) superimposed on a map of δ^3He (in %) interpolated to 1100 m depth. This is similar to that originally presented by Lupton (1996). Gray dots indicate historical stations used for mapping (see Section 1). Other stations nearby but outside of the displayed area were also used in the mapping. The δ^3He contour (white lines) interval is 2%, or about ten times sample measurement errors. ***b, Inset showing neighboring stations close to the Loihi Seamount, close to the Island of Hawaii*** with bottom topography in gray scale, contour interval is 1000 m, islands are black and ***c, meridional section of 1100 m depth δ^3He (in %) along ∼152° W***. Red stars are from the GP15 (2018) section and black dots are historical data dating from 1985 through 2015 (Jenkins et al., 2019a). Error bars represent 1 standard deviation uncertainty due to measurement and interpolation errors. (For interpretation of the colors in the figure(s), the reader is referred to the web version of this article.)

of the helium isotope ratio anomaly (δ^3He, defined in Eq. (1) in Section 2) interpolated to 1100 m depth in the central to eastern North Pacific. Historical data (publicly available, Jenkins et al., 2019a; Lupton, 1998), indicated by gray dots, extend back to the 1980s and are used to enhance spatial coverage. The contoured δ^3He field shows the largely eastward influence of the mid-depth volcanic ^{3}He tongue first described and documented by Lupton (1996). The location of the nearest four stations, including the hydrocast directly over the Loihi Seamount are shown in the inset (Fig. 1b). The 1100 m δ^3He signature for stations along ∼152°W (Fig. 1c) shows that the feature has a well-defined meridional extent that it has persisted for many decades.

2. Methods

Water samples were taken for helium isotope and noble gas measurements using a 36 place, ∼10 liter Niskin bottle rosette. The samples were drawn within a few minutes after the bottle was vented *via* TYGON tubing to a 76 cm length of 1.6 cm outer diameter refrigeration grade copper tubing that was isolated with pinch clamps and immediately crimp-sealed (Young and Lupton, 1983) for shore-based analysis. The samples were quantitatively gas-extracted and mass-spectrometrically analyzed for helium isotope ratios and noble gas abundances referenced to a marine atmospheric standard (Jenkins et al., 2019b). We report isotope ratio anomalies relative to the atmosphere according to

$$\delta^3\mathrm{He} = 100 \times \left(\frac{\left[{}^3\mathrm{He}/{}^4\mathrm{He}\right]_\mathrm{X}}{\left[{}^3\mathrm{He}/{}^4\mathrm{He}\right]_\mathrm{A}} - 1 \right) \% \qquad (1)$$

where the subscript X refers to the sample, and A to air. Uncertainties depend on a combination of ion-counting statistics and instrument stability. They range from ∼0.15% for samples close to the atmospheric ratio, up to ∼0.4% for the highest ratios observed. Dissolved helium and neon concentrations were measured using quadrupole mass spectrometric peak-height manometric techniques (Jenkins et al., 2019b; Stanley et al., 2009) and are reported as saturation anomalies, defined (e.g., for helium) as

$$\Delta\mathrm{He} = 100 \times \left(\frac{C\,(\mathrm{He})}{C_S\,(\mathrm{He})} - 1 \right) \% \qquad (2)$$

where C and C_S are the measured and solubility concentrations of helium (or neon). The solubility concentrations are a function of temperature and salinity (Jenkins et al., 2019b). The other noble gases (Ar, Kr, and Xe) were also measured on these samples as a quality check; but are not reported here. Helium and neon concentrations were determined to an accuracy of approximately 0.15%. For both the Loihi Seamount and Puna Ridge stations, most helium isotope and noble gas samples were measured in replicate and average values are reported. In all cases, reproducibility between replicates was close to expected errors. Pooled standard deviations for δ^3He, ΔHe, and ΔNe replicates were 0.22%, 0.29%, and 0.28% respectively, which represents the convolution of all sampling and analytical errors. It should be mentioned that the δ^3He and ΔHe statistics are impacted (increased) due to the anomalously large hydrothermal signals.

To determine the isotopic nature of the non-atmospheric helium, we account for the two primary atmospheric components of helium: that portion dissolved during air-sea gas exchange, and that fraction introduced by hydrostatic compression of bubbles introduced by wave action at the sea surface. The former can be accounted for using helium isotope solubility fractionation measurements (Benson and Krause, 1980) and noble gas solubility functions (Jenkins et al., 2019b). The latter is estimated using an em-

pirical relationship with near-surface neon saturation anomalies, since neon is similarly affected by air injection processes. The amounts of excess helium isotopes are calculated (Jenkins et al., 2018) using

$$C_{XS}\left(^4\mathrm{He}\right) = C_M\left(^4\mathrm{He}\right) - C_S\left(^4\mathrm{He}\right) - 0.22\left(C_M\,(\mathrm{Ne}) - C_S\,(\mathrm{Ne})\right) \tag{3}$$

and

$$C_{XS}\left(^3\mathrm{He}\right) = R_A\Big[\left(1+\delta^3\mathrm{He}/100\right)C_M\left(^4\mathrm{He}\right) - \alpha_E C_S\left(^4\mathrm{He}\right) - 0.22\left(C_M\,(\mathrm{Ne}) - C_S\,(\mathrm{Ne})\right)\Big] \tag{4}$$

where the subscripts S and M signify solubility equilibrium and measured values respectively, R_A is the atmospheric helium (^{3}He/^{4}He) isotope ratio (Clarke et al., 1976), and α_E is the solubility helium isotope effect (Benson and Krause, 1980). They are further corrected for a slight (~0.2 and ~0.3% for He and Ne respectively) enhancement in saturation anomaly at these depths resulting from diapycnal mixing effects (Jenkins et al., 2018).

For the Loihi Seamount station, trace metals were determined shipboard on water from the same Niskin bottles using FIA (Flow Injection Analysis) in order to avoid questions of colocation due to short term time and space scale variability between hydrocasts. The samples were filtered through 0.8/0.45 µm Pall ACROPAK 500 capsules that had been pre-cleaned by soaking three days with 10% hydrochloric acid (1.2 M HCl) and flushed with 3-5 L of Milli-Q water, and stored refrigerated between casts. The capsule filter was pre-flushed with 0.5-1 L of unacidified seawater. The filtered seawater samples were acidified to pH 2 using sub-boiling distilled hydrochloric acid. Although the samples were drawn from a non trace-metal clean Niskin rosette, the Fe and Mn values are much larger than measured contamination levels for this system, as deduced from contemporaneous comparison with the trace-metal-clean system elsewhere.

Due to much lower metal concentrations elsewhere, the U.S. GEOTRACES trace-metal clean CTD carousel (GTC) was used for trace metal sampling for the other stations. This sampler has a plastic-coated aluminum frame, titanium pressure housings for electronics and sensors, no sacrificial zinc anodes, and 24 ×12 liter General Oceanics GO-FLO bottles modified for trace metal sampling (Cutter and Bruland, 2012). Before deployment and immediately upon recovery, the tops and bottoms of the GO-FLO bottles were covered with polyethylene shower-caps, and the bottles were removed from the frame and carried into the U.S. GEOTRACES clean container laboratory for sub-sampling. The GO-FLO bottles were pressurized to 6 psi using 0.2 µm HEPA-filtered compressed air, and samples were passed through 0.2 µm Pall ACROPAK SUPOR filter capsules that had been pre-cleaned by soaking overnight and flushed with 5 L of unacidified seawater. Samples of the 0.2 µm-filtered seawater were collected following three bottle rinses for shipboard analyses and for shore-based inductively-coupled plasma mass spectrometry (ICP-MS) analyses. The shipboard samples were drawn into acid pre-washed 125 mL polymethylpentene bottles and immediately acidified to 0.006 M hydrochloric acid (HCl) using sub-boiling distilled HCl. The ICP-MS samples were drawn into 250 mL low density polyethylene bottles and acidified to 0.024 M HCl (Optima, Fisher).

For shipboard dissolved metal analysis, the sample bottles were stored in polyethylene bags in the dark at room temperature before analyses, usually within 24 h of collection. Prior to analysis, samples for dissolved iron (dFe) and manganese (dMn) were microwaved in groups of 4 for three minutes at 900 W to 60 ± 10 °C in an effort to release dFe from complexation in the samples. Samples were allowed to cool for at least 1 h prior to FIA. Dissolved Fe and Mn were determined subsamples using methods of Measures et al. (1995) for dFe and Resing and Mottl (1992) for dMn. Samples were analyzed in groups of 8, and the samples collected at each station were generally analyzed together during the same day. Detection limits and precisions were 0.071 nM and 1.9% relative standard deviation at 1.4 nM for Fe, and 0.15 nM and 9.7% relative standard deviation at 0.51 nM for Mn. We converted FIA results, normally reported in nM units, to nmol kg^{-1} in this paper by dividing by the density of the seawater at 20 °C and its measured salinity.

Iron and manganese were extracted from the seawater samples for ICPMS analysis and pre-concentrated 25x using a SeaFAST pico-automated system (Elemental Scientific), following isotope spiking with ^{57}Fe and buffering to pH ~6.2, using an offline-modified version of Lagerstrom et al. (2013), as reported by Jensen et al. (2020). Extracts were analyzed at medium resolution on a Thermo Element XR ICP-MS. Iron was quantified using isotope dilution, and Mn using matrix-matched standard curves that were set to match the concentration range of the samples. All samples exceed the detection limits of 0.036 nmol kg^{-1} and 0.002 nmol kg^{-1} for Fe and Mn respectively. External accuracy was confirmed by replicate analyses of the GSC-2 seawater solution, which were found to have concentrations of 1.631 ± 0.072 nmol kg^{-1} for Fe and 2.140 ± 0.129 nmol kg^{-1} for Mn ($n = 6$ each), statistically indistinguishable from consensus concentrations (1.535 ± 0.115 nmol kg^{-1} and 2.180 ± 0.075 nmol kg^{-1}, respectively).

At the Loihi station, comparison of FIA and ICP-MS results show good agreement when both were sampled from the same bottles in the GTC cast and fall on a 1:1 line (Fig. 2a) with the exception of one sample, which may have been contaminated. Comparison of FIA and ICPMS results for the neighboring stations (Fig. 2b) also show good agreement. However, at Loihi, only FIA metal analyses were done on the Niskin casts (black symbols/lines) where ^{3}He was also collected. As discussed in Section 3.1, there was a pronounced difference in light transmission between the two casts below 1200 m that indicates a significant difference in hydrothermal influence on the sampled waters between casts.

Dissolved methane was determined using a headspace equilibration-cavity ring-down spectroscopy method (Roberts and Shiller, 2015). Samples were collected immediately after the other dissolved gas samples, equilibrated with methane-free zero-air, and head-space methane determined using a Picarro G2301 Greenhouse Gas Analyzer. Calibration was performed using both methane-free zero air and a 5 ppmv CH_4 gas standard. Variability of dissolved methane in deep ocean samples from the GP15 section suggests a standard deviation of better than 0.06 nmol kg^{-1} on samples of ~0.6 nmol kg^{-1}, similar to the results of Roberts and Shiller (2015).

We also characterized hydrothermal input by determining total dissolved sulfides (TDS) and pH. TDS samples were collected using the GTC, filtered through the same 0.2 µm capsules as the metal samples, and stored in 4 liter cubitainers. Filtered water samples were transferred to glass stripping vessels, acidified to a pH of 1.6 and analyzed at sea usually within 8 h of collection using cryogenic trapping and GC/flame photometric method (Radford-Knoery and Cutter, 1993) in duplicate. This method quantifies total dissolved sulfide as free ions and metal-sulfide complexes with a 0.2 pM detection limit. To determine pH at each depth, 60 mL of filtered water were subsampled from the GTC using a syringe and thee-way valve. This water was hermetically transferred into an automated Ocean Optics UV-VIS spectrophotometric system, pure m-cresol purple added, and absorbance measured at three wavelengths (Carter et al., 2013; Clayton and Byrne, 1993). These samples were usually analyzed within 2 h of collection.

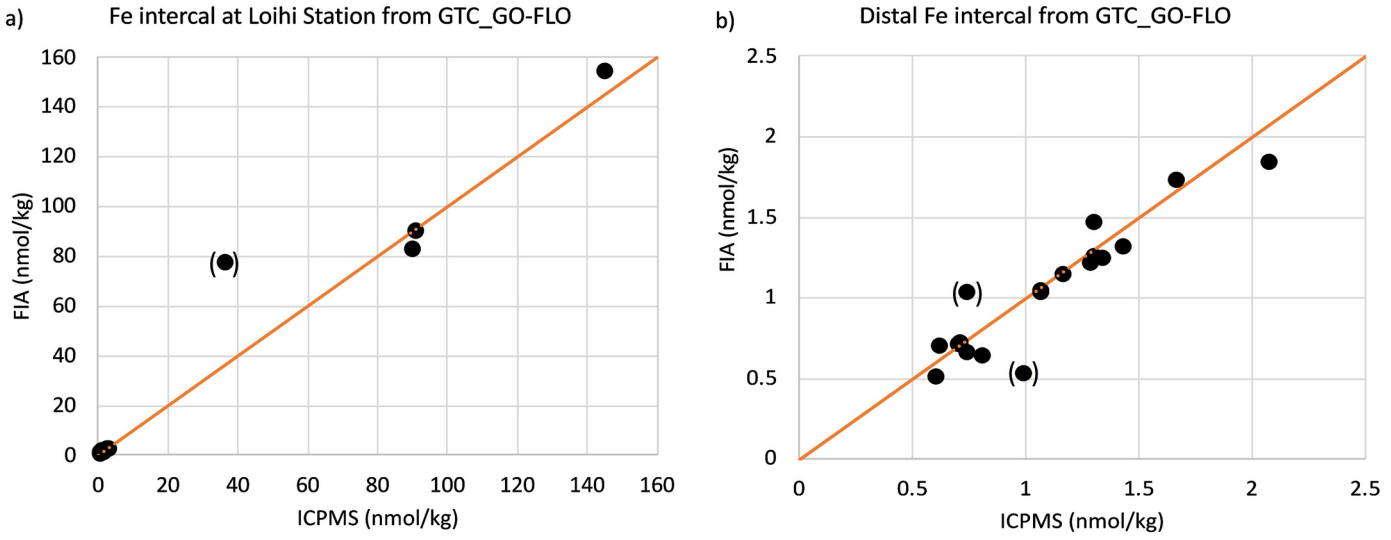

Fig. 2. Inter-calibration of dissolved Fe measurements drawn from the same (GTC) bottles made by shipboard FIA (y-axis) and ICPMS (x-axis) for the **(a) the Loihi hydrocast** and for **(b) neighboring ("distal") stations** (Stations 14, 16, 18, 19, 21, and Puna Ridge). The orange lines have an intercept of zero and unit slope.

3. Results and metal-^{3}He ratios

3.1. The Loihi station

The station over the Loihi Seamount was located at 18°54'23"N, 155°15'29"W, with a nominal depth of 1300 m, directly above the center of Pele's Pit (Clague et al., 2019), a collapse feature resulting from a 1996 seismic/eruption sequence (Duennenbier et al., 1997). The target sampling location was within ~100 m of three active hydrothermal vents (Tower, Hiolo, and Spillway) to its southeast, and ~300 m of a shallower vent (Lohiau at about 1150 m depth) to the north-northwest (Bennett et al., 2011; German et al., 2018). Measured isotope and element profiles for samples drawn from the Niskin hydrocast are shown in Fig. 3 (a-f), along with properties measured on the GTC casts (g-j), as well as the calculated profiles of excess helium isotopes (Fig. 3k-l) and their isotopic relationship (Fig. 3m). Except for neon and methane, all elements and isotopes from the Niskin hydrocast show the same structure below 1000 m, with maxima ~100 m above the sea floor and elevated concentrations extending ~200 m above. The GTC hydrocast measurements exhibit the continued increase in signal to the seafloor (red lines/symbols in Fig. 3g-h). The trend is also seen in the total dissolved sulfide (Fig. 3i) and mirrored by the pH (Fig. 3j), further reflected in a decrease in light transmissivity below 1250 m (not shown). The differences between the two hydrocasts, despite precise ship positioning is expected because a modest 5° difference in wire angle can result in a ~100 m lateral displacement package toward or away from the three nearby active hydrothermal vents in Pele's Pit.

Helium isotope ratio anomalies (Fig. 3a) approaching 400% were observed, comparable to earlier observations at Loihi (Lupton, 1996). Corresponding to this maximum was a ~22% peak in helium saturation anomalies (Fig. 3b), in contrast to neon, which showed no difference from other stations. The small ΔNe excess at 1100 m is likely a sampling artifact producing a miniscule bias in the helium, further corrected for by the isotope calculations. Thus, the helium supersaturations are non-atmospheric. Like Lupton (1996), we find the isotopic ratio of the Loihi helium to be substantially elevated compared to typical Mid Ocean Ridge (MOR) sources (27.3 $\pm$ 0.3 R_a *vs* ~8 R_a where R_a is atmospheric ratio 1.384×10^{-6}) (Clarke et al., 1976)). Our result is slightly higher than Lupton's (1996) originally reported 23.5 R_a. (We contend that Lupton inappropriately included near-surface waters as endmembers, which flattens the slope slightly). Our ratio is more consistent with observations of Loihi summit lavas (Kaneoka et al., 1983; Kurz et al., 1983; Rison and Craig, 1983), a signature of primitive mantle volatiles associated with the leading edge of the Hawaiian hot spot (Kurz et al., 1982, 1983).

The temperature data for this station revealed no detectable thermal signature at the depths of ^{3}He anomalies, consistent with the very high ^{3}He:heat ratios reported for the Loihi seamount by Lupton et al. (1.1 fmol J^{-1}) (1989). This contrasts with ratios at least two orders of magnitude smaller for mid-ocean ridge (MOR) systems (see Elderfield and Schultz, 1996; Lupton et al., 1989). This difference results from the profound geo-tectonic differences between a mid-plate mantle-plume fueled volcano in the shield-building stage and MOR spreading centers. While MOR have characteristically shallow magma chambers (~1 km below seafloor), Loihi's magma chamber is ~10 times deeper, providing greater opportunity for decoupling between primary volatiles like ^{3}He and heat (cf. Hofmann et al., 2011).

High concentrations of dissolved methane are commonly observed in hydrothermal vent waters and appear to be derived from reduction of CO_2 to CH_4 under conditions associated with plutonic rocks and temperatures of ~300-400 °C (Wang et al., 2018). For the Loihi profile, the enrichment in CH_4 is modest, less than 1 nmol kg^{-1} relative at similar depths at other stations in the region (~1 nmol kg^{-1}, Fig. 3f. These values are significantly lower than the roughly 5-15 nmol kg^{-1} reported by Gamo et al. (1987) prior to the 1996 seismic/volcanic events and the collapse of Pele's Vents. In contrast, dissolved methane in other hydrothermal end-member solutions are often in the micromolar to millimolar range. Because the processes of formation of hydrothermal methane are different from the generation of hydrothermal ^{3}He or Fe, we don't necessarily expect broad oceanic correlation of methane with these other hydrothermal parameters. Nonetheless, the comparison is potentially instructive. For our two most methane-enriched Loihi samples, we observe $xsCH_4/C_{XS}(^3He)$ molar ratios of $\sim 5 \times 10^4$, much smaller than the $\sim 5 \times 10^5$ ratio reported by Gamo et al. (1987). Here we define $XSCH_4$ as the amount of methane above values observed at comparable depths away from Loihi. In far greater contrast, Keir (2010) reported $xsCH_4/^3$He ratios in mid-ocean ridge hydrothermal samples that were 10-1000-fold higher than our value. Likewise, the $xsCH_4$/Fe ratios of our two most methane-enriched samples are much lower than $xsCH_4$/Fe ratios observed in most other vent fluids (e.g., Charlou et al., 2002). This suggests that either the Loihi methane had been rapidly consumed

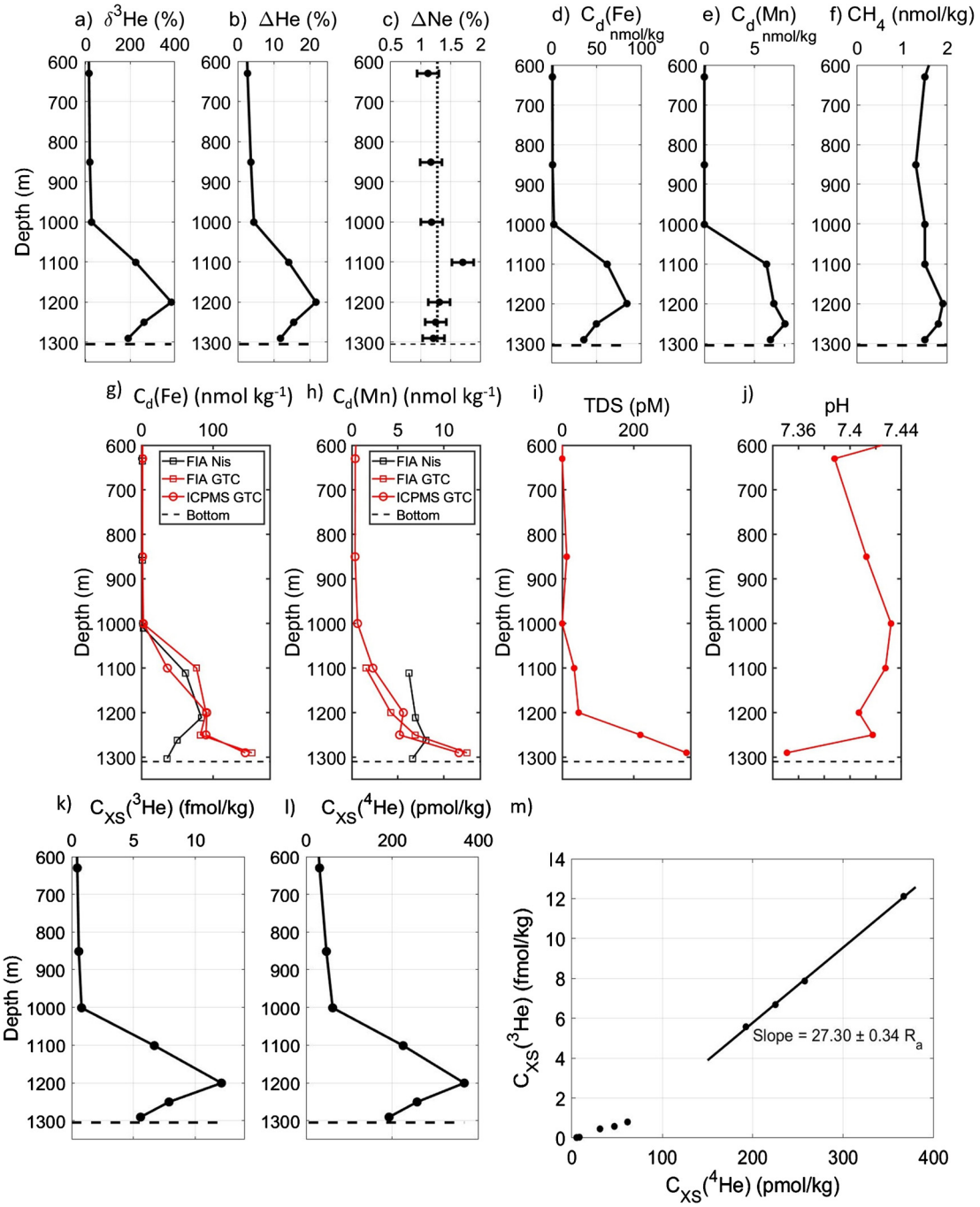

Fig. 3. Loihi profiles of **a)**, helium isotope ratio anomaly δ^3He in %, **b)**, dissolved helium saturation anomaly in %, **c)**, dissolved neon saturation anomaly in %, **d)**, dissolved Fe in nmol kg^{-1}, **e)**, dissolved Mn in nmol kg^{-1}, **f)**, dissolved CH_4 in nmol kg^{-1}, **g)** dissolved Fe (ICPMS for GTC hdyrocast only, and FIA for both), **h),** dissolved Mn (same as Fe), **i),** TDS (pM) from the GTC cast, **j)**, pH from the GTC cast **k)**, excess ^{3}He in fmol kg^{-1}, **l)**, excess ^{4}He in pmol kg^{-1}, and **m)**, correlation between excess ^{3}He and ^{4}He. The dashed line represents the bottom depth at the sampling location.

by methanotrophs during transport and dilution from the vents to our sampling location, or that the Loihi system is nearly devoid of methane. Indeed, basalt-hosted vent systems tend to have lower methane concentrations in their hydrothermal fluids than do ultramafic hosted systems (Keir, 2010), though their $xsCH_4/^3He$ ratios still tend to be 10-100-fold greater than what we observe.

The maximum dFe and dMn concentrations measured for both hydrocasts at Loihi station (Fig. 3d-e and g-h) were roughly half of those reported earlier by Bennett et al. (2011) for Pele's Pit. This could be due to spatial variations (see previous discussion in methods), but German et al. (2018) have described a gradual, decade time-scale decrease in vent temperatures at Loihi. Nonetheless, the maximum dFe is about 7 times larger than observed directly over the southern East Pacific Rise (SEPR) (Fitzsimmons et al., 2017; Resing et al., 2015), while the dMn is roughly twofold smaller.

The overall slope of the "proximal" Fe:^{3}He relationship within Pele's Pit was $7.4 \pm 0.5 \times 10^6$ (Fig. 4a), surprisingly similar to the SEPR. Since the published SEPR relationship (Resing et al., 2015) was based on preliminary shipboard dFe measurements, we use the average of shore-based ICP-MS measurements within 50 m of the core of the ^{3}He maximum for the station over the SEPR (Schlitzer et al., 2018) to obtain a revised proximal SEPR Fe:^{3}He ratio of 7.6×10^6, virtually identical to Loihi. This is remarkable since the overall dFe and ^{3}He concentrations at the two sites are

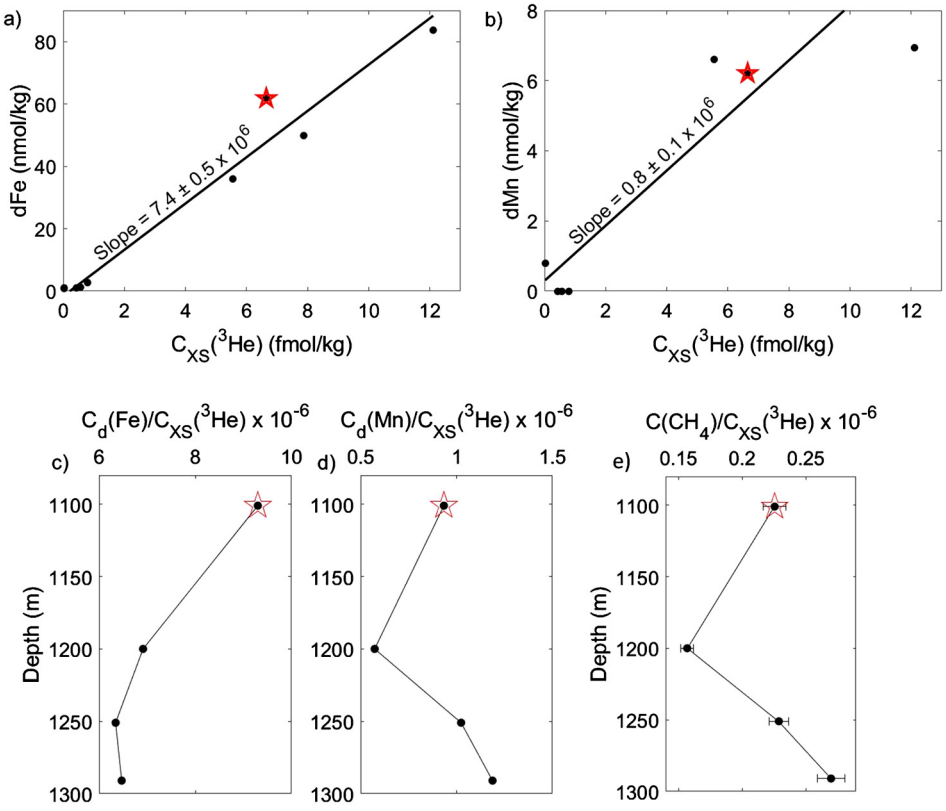

Fig. 4. The observed correlations at the Loihi station between excess ^{3}He in fmol kg^{-1} and **a**, dissolved Fe and **b**, Mn, both in nmol kg^{-1}, and **c-d, molar ratio profiles** of dissolved Fe, Mn, and **e** methane **to ^{3}He**. Note the shallowest plume values (red star) which likely represent ratios "exported" from the site.

so different, and the processes leading to their creation are completely decoupled. That is, the dFe enrichment at Loihi is derived from low-temperature leaching of basalt by hotspot-derived volcanic carbon dioxide, which drives down the pH of Loihi fluids (Sedwick et al., 1992). In contrast, the dFe enrichment at mid-ocean ridge systems such as SEPR is dependent on hot (>300 °C) reactions of acidic fluids with Fe silicates in basalts (Von Damm, 1985).

The overall Mn:^{3}He relationship (Fig. 4b) is $0.8 \pm 0.1 \times 10^6$, more than twofold smaller than observed at the SEPR (Resing et al., 2015). The depth profiles of the Fe:^{3}He ratio, shown in Fig. 4c, is highest ~100 m above the plume's core. In contrast, the Mn:^{3}He ratio profile, shown in Fig. 4d, shows an increase below the core, resembling more the CH_4:^{3}He ratio profile shown in Fig. 4e. Although divergence of the Fe:^{3}He profile below the core of the ^{3}He maximum could result from *in situ* scavenging, consideration of the detailed bathymetry and nearby vent locations in relation to the sampling site (e.g., see Fig. 1b of Bennett et al., and 4b of Clague et al. Bennett et al., 2011; Clague et al., 2019), suggests that the profiles are the composite signature of multiple hydrothermal sources at different locales and depths in and near Pele's Pit. Moreover, since the sill depth of Pele's Pit is ~1100 m, the metal:^{3}He ratios that are exported to influence surrounding open ocean waters are likely the values at or near the 1100 m depth. Thus, we adopt the somewhat higher values of $9.3 \pm 0.3 \times 10^6$ and $0.93 \pm 0.04 \times 10^6$ for the molar Fe:^{3}He and Mn:^{3}He ratios that escape to feed the regional-scale "hydrothermal tongue".

3.2. *The "distal" stations*

The GEOTRACES GP15 δ^3He and dFe profiles (Fig. 5) showed distinct maxima at 1100 m depth for the stations within 500 km of Loihi (18, Puna Ridge, and 19), while more remote "background" stations (14, 16, and 21), falling outside of the main Loihi plume (Fig. 1a and 1c) do not exhibit discernible features. Concentrations of excess ^{3}He, dFe, and dMn at all six stations were interpolated to the 1100 m depth, and decrease monotonically with distance from Loihi (Fig. 6a-c), with the exception of station 14 where dFe and dMn appear elevated (and dissolved oxygen more depleted) due to the influence of the North Pacific oxygen minimum zone. There, a secondary subsurface maximum of reduced metals such as Mn(II) is present due to their redox stability under suboxic conditions (Johnson et al., 1996).

The dissolved metal relationships to ^{3}He are plotted in Fig. 6d and 6e. We invoked a linear dFe:^{3}He relation because the data at the critical intermediate concentrations were insufficient in number to distinguish from a non-linear relationship. Included in the plot is an exponential regression (dashed line) that fits the data well, but has only one degree of freedom in the fit. The linear dFe:^{3}He regression slope for the five distal stations is $4.4 \pm 0.9 \times 10^6$, about a factor of two lower than the proximal ratio of $9.3 \pm 0.3 \times 10^6$. This decrease in slope is comparable to that observed over the SEPR (Fitzsimmons et al., 2017). At Loihi, the proximal relationship arises from non-conservative dFe losses during plume transport, which could include abiotic scavenging of Fe(II) but also may include microbial Fe utilization, given the rich Fe-oxidizing microbial communities known to exist in Loihi microbial mats (Emerson and Moyer, 2002; Emerson et al., 2007). The distal dMn:^{3}He relationship (Fig. 6e) of $0.9 \pm 0.1 \times 10^6$ (excluding Station 14, which is largely unaffected by Loihi) appears equal to the proximal ratio, which is consistent with SEPR (Fitzsimmons et al., 2017) and earlier studies (James and Elderfield, 1996) that dMn behaves conservatively in the non-buoyant hydrothermal plume.

The similarity of both proximal and distal dFe:^{3}He ratios between the Loihi and SEPR is remarkable for two reasons. First, ^{3}He is a primary volatile that is strongly partitioned out of the parent magma while dFe is affected by water-rock exchange, chemical

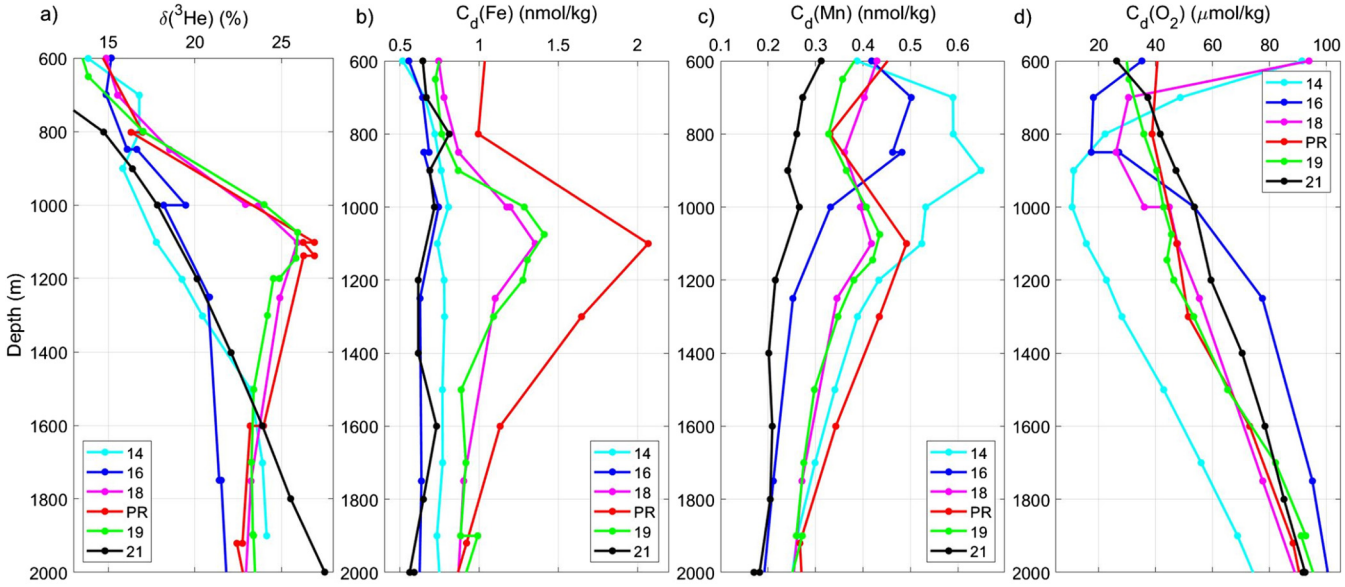

Fig. 5. Composite depth profiles at the distal stations of **a**, δ^3He in %, **b**, dissolved Fe in nmol kg^{-1}, **c**, dissolved Mn in nmol kg^{-1}, and **d**, dissolved oxygen in μmol kg^{-1} for the more distant stations shown in Fig. 1 (not including the Loihi station). From north to south they are station 14 (cyan), 16 (blue), 18 (magenta), Puna Ridge (red), 19 (green), and 21 (yellow). Note the pronounced maxima in δ^3He, dFe, and dMn at 1100 m depth identified in δ^3He by Lupton (1996) as the Loihi plume for the "nearby" stations (Puna Ridge, 18, and 19). Also, note the aberrant behavior for the dMn (and to a lesser extent dFe) for station 14.

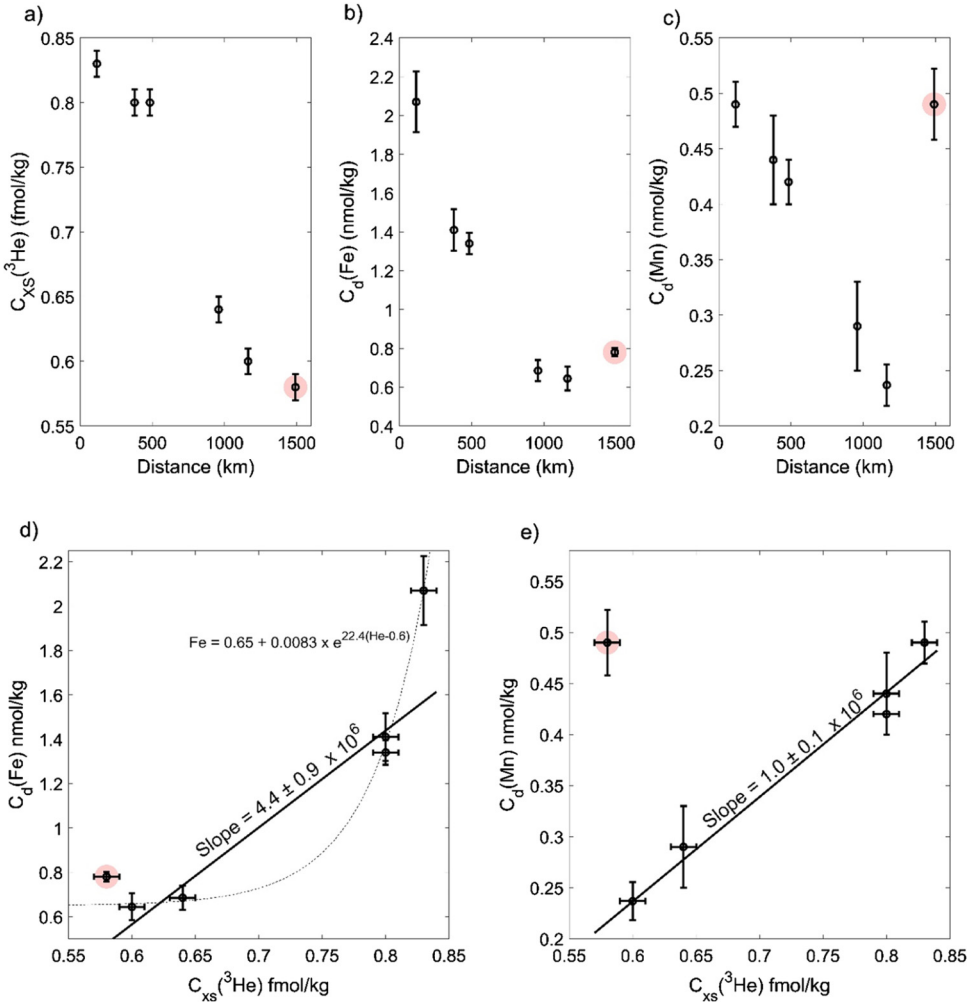

Fig. 6. The distal excess ^{3}He, dissolved iron, and manganese concentration variation vs. distance from Loihi for **a.** excess ^{3}He in fmol kg^{-1}, **b.** dissolved Fe in nmol kg^{-1}, and **c.** dissolved Mn in nmol kg^{-1}. **Correlation with excess ^{3}He** for **d.** dissolved Fe and for **e.** dissolved Mn. Error bars, which combine analytical and interpolation uncertainties, are 1 σ for both variables. The solid lines are from type-II weighted linear regressions (excluding station 14, highlighted in pink for Fe and Mn). The dashed line in **d** is an exponential fit for comparison.

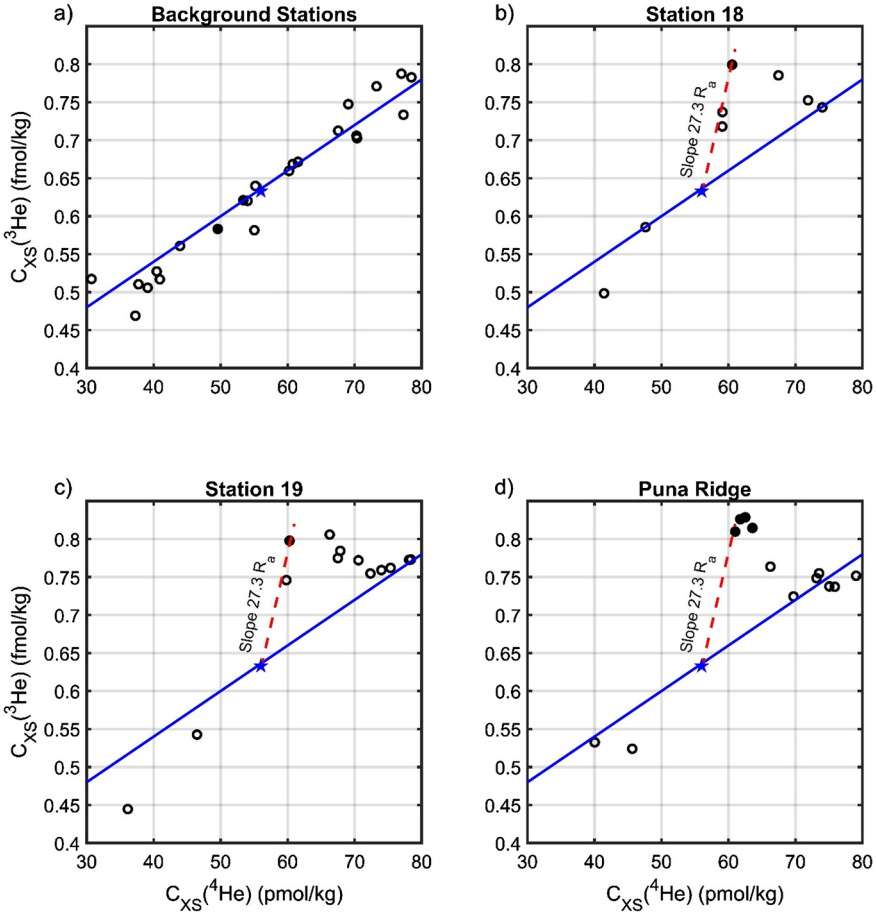

Fig. 7. The mid-depth excess helium isotopes relationships for the background and three nearest stations. The filled circles correspond to samples close to 1100 m depth. **a** Stations 14,16, and 21 are considered "background" and the blue line, which falls through these points is for reference only. **b-d** are for the three closest stations (18, 19, and Puna Ridge, see Fig. 1a). The blue star is the estimated unperturbed 1100 m value and the red dashed line's slope corresponds to the isotopic composition of Loihi plume helium (see Fig. 2i).

precipitation, microbial transformation, and the presence/absence of binding ligands. Thus, given these very different geochemical supply mechanisms to hydrothermal fluids, it is remarkable that Fe and ^{3}He would produce similar ratios in different vents. Second, Loihi and the SEPR have vastly different geochemical, geological, hydrothermal, and tectonic characteristics, making it even more unlikely that Fe and ^{3}He would have similar ratios. The SEPR is a mid-ocean ridge spreading center with a shallow (~1 km depth) magma chamber, tholeiitic basalts, and high temperature hydrothermal vent fluids, while Loihi is a mid-plate, mantle plume-driven shield-building volcano with a deeper (~10 km depth) magma chamber, and lower temperature hydrothermal vent fluids (German et al., 2018; Rouxel et al., 2018). Furthermore, SEPR vents have millimolar concentrations of H_2S (Von Damm et al., 2003), which should minimize dFe concentrations due to precipitation of iron sulfides (Feely et al., 1996, 1987). We observed less than nanomolar TDS concentrations at Loihi and only modest acidification, minimizing dFe removal.

In contrast to both Loihi and the SEPR, recent observations in the North Atlantic TAG hydrothermal plume show dFe concentrations (Fitzsimmons et al., 2015) of ~60 nmol kg^{-1} with a corresponding ^{3}He excess (Jenkins et al., 2015) of ~0.6 fmol kg^{-1}, leading to a molar Fe:^{3}He ratio close to 100×10^6. This is about ten to fifteen times higher than observed here and at the SEPR. Observations over the southern Mid-Atlantic Ridge at around 13°S yield a similarly high value of $\sim 70 \pm 30 \times 10^6$ according to Saito et al. (2013). Thus, there appears to be a greater Atlantic-Pacific disparity in dFe:^{3}He ratios than between mid-ocean ridge and mid-plate mantle plumes within the Pacific. This verifies that there are numerous factors fixing the persistent Fe:^{3}He ratio supplied to the ocean by any single hydrothermal vent, including tectonic context, depth of the magma chamber (and subsequent temperature at venting), host rock composition, microbial composition, and bottom water conditions (especially oxygenation). The numerical prediction of ^{3}He and persistent dFe fluxes from hydrothermal vent fluids is a complex task. We attempt to quantify those fluxes here for Loihi Seamount.

4. Estimating the hydrothermal ^{3}He flux

Loihi's uniquely high ^{3}He/^{4}He signature provides an unambiguous and quantitative measure of the amount of excess ^{3}He attributable to Loihi at each station, as distinct from the regional "background" of volcanic and radiogenic helium emitted by more distant vents and sediments. In Fig. 7 we show the relationships between excess ^{3}He and ^{4}He for the more distant "background" stations (14, 16, and 21 in Fig. 7a) and the three stations near Loihi (18, 19, and Puna Ridge in Fig. 7b-d). In the neighboring stations, there is a clear deviation from the background slope defined by the more distant stations that allows us to quantitatively separate out the Loihi contribution. In all panels, the shallowest points are on the left and deepest points on the right of the graphs. The blue line references the background trend and the blue star represents a "best guess unperturbed" $^3He_{XS}$-$^4He_{XS}$ composition for the 1100 m depth. In the other panels, the red dashed line corresponds to the unique ^{3}He/^{4}He trend line associated with the Loihi

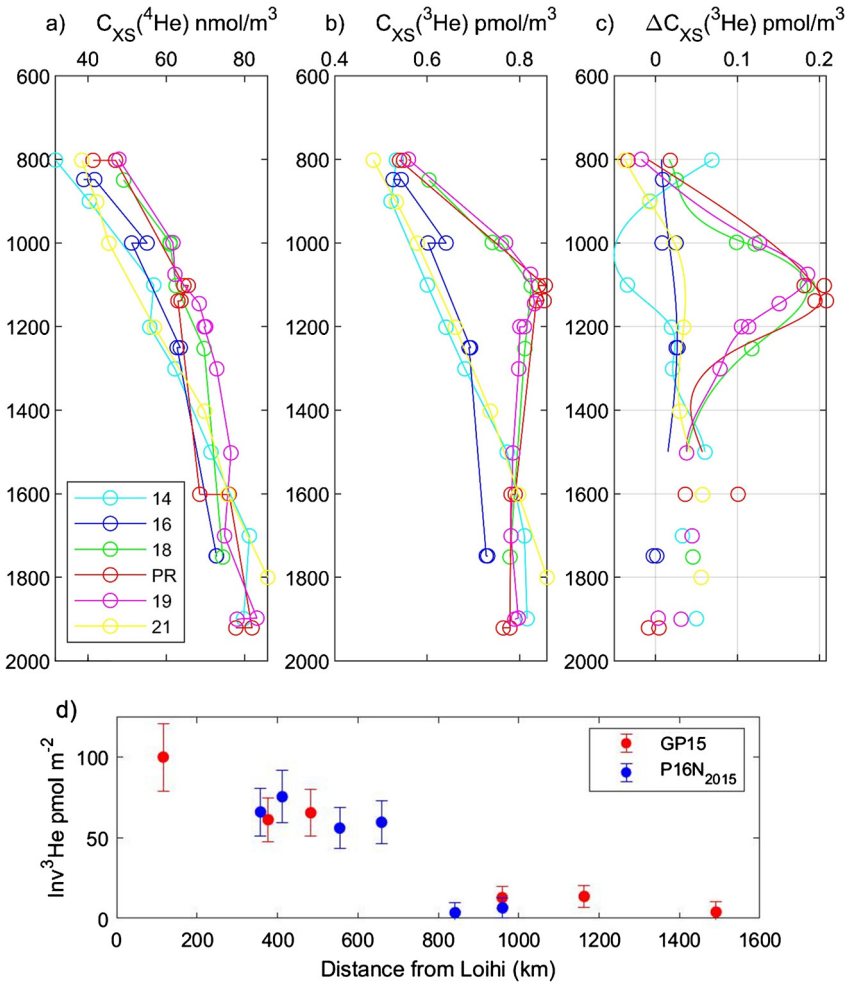

Fig. 8. Profiles of a) excess ^{4}He in nmol m^{-3}, b) excess ^{3}He in pmol m^{-3}, and c) Loihi-linked excess ^{3}He in pmol m^{-3} for six GP15 stations. The solid lines in c) are smoothing spline fits to all data in each profile. We only integrated over the depth range of integration (900 to 1300 m). **d) Computed ^{3}He inventories in pmol m^{-2} for stations along ~152°W vs. distance from Loihi**, including both GP15 and the recent 2015 occupation of P16N.

mantle plume signature (27.3 R_a), which demonstrates convincing evidence that the 1100 m features (filled circles) arise from the Loihi source. This gives us a quantitative method for defining and integrating the water column excess ^{3}He attributable to the Loihi source.

Fig. 8a and 8b show the excess helium isotope profiles for the GP15 stations, calculated using equations (3) and (4), and Fig. 8c shows the Loihi-sourced ^{3}He profile as estimated by subtracting the average of "background" station profiles between 5 and 10°N (station 21) and between 30 and 35°N (stations 14 and 16). The helium isotope profiles nearest Loihi exhibit a significant ^{3}He signature between 900 and 1300 m depth with a maximum near 1100 m. The large vertical spread may be due in part to the topographic distribution of the many hydrothermal vent sites (Bennett et al., 2011; Clague et al., 2019; Rouxel et al., 2018) at Loihi. In addition, although diapycnal mixing in the open ocean is weak (Ledwell et al., 1998, 1993), seamounts are known sites of enhanced vertical mixing (Lueck and Mudge, 1997; Toole et al., 1997). We thus argue that the vertical spread likely occurs as a result of both vertically distributed sources and enhanced vertical mixing in the vicinity of the injection sites.

We model the regional distribution of the vertically integrated ^{3}He anomaly (the inventory) between 900 and 1300 m depths using the observations reported here along with selected historical profiles. Uncertainties are assigned as a combination of analytical precisions and interpolation errors. The latter, estimated by assuming a profile shape intermediate between a box-car (a constant value over the range) and a triangular distribution dominates. The inventories, which include results from a recent occupation along this meridian (P16N in 2015) show a smooth trend *vs.* distance (see Fig. 8d), supporting the idea that the feature described is persistent. Using historical data, we can further develop a picture of the distribution of the vertically integrated Loihi-sourced ^{3}He anomaly. For those profiles with contemporaneous neon concentration measurements, similar calculations can be done, but for those without neon data (notably the more distant WOCE P17N section at 135°W) a much more approximate scheme (Jenkins et al., 2018) must be used, with significantly less accuracy.

This model rests on the assumption that the existence of a persistent regional ^{3}He feature emanating from Loihi requires a sustained hydrothermal flux of this isotope. The magnitude of the required flux depends on the regional scale velocity and turbulent diffusion responsible for its dispersion. We use an idealized advection-diffusion model to set approximate constraints on this flux. We constructed a two-dimensional rectangular slab-channel model for this depth range, spanning from the dateline to 120°W and between 10° and 30°N. We impose a uniform zonal velocity and a spatially variable but isotropic horizontal turbulent diffusivity. Horizontal resolution is 25 km, and a standard, mass-conserving, upwind-differencing algorithm (Glover et al., 2011) is used to integrate the model to steady-state. Choice of the zonal velocity is critical in that the results will scale almost linearly with it.

We use a velocity of 0.0040 ± 0.0016 m s^{-1} obtained for this location and depth from a global multi-tracer data assimilation model calibrated by radiocarbon and CFCs (Schlitzer, 2004, 2007) which has been used successfully to model regional/global distributions of radiocarbon and ^{3}He (Schlitzer, 2007, 2016). This velocity is consistent with a recent analysis of circulation at 1000 m depth from float data by Ollitrault and De Verdiere (2014, their Fig. 12), and we conservatively estimate an uncertainty of 40% to this value. The presence of the Hawaiian Island chain in the path of this zonal current may lead to spatial enhancement of lateral diffusion (e.g., Chen et al., 2015). Thus, we impose a simple spatial structure on the lateral diffusivity as the sum of a constant background diffusivity plus a half sine function centered on 20°N, 150°W whose value is zero at 10° and 30°N, and at 180° and 120°W. The magnitudes of the background and amplitude diffusivities were treated as variables to be optimized against observations.

To constrain the model, we compute integrated water column inventories between 800 and 1300 meters depth of the Loihi-attributed ^{3}He (based on the ^{3}He/^{4}He anomalies and calculations described above) using only the more recently occupied stations (2015 and 2018) that have noble gas measurements along the 152 °W section. For the 135°W section, due to the lack of noble gas data, we use a less precise calculation (Jenkins et al., 2018) using the historical helium isotope measurements largely made by Lupton (1996, 1998). For weighting purposes, we estimated uncertainties in these inventories due to the combination of measurement and interpolation/integration errors.

We embedded the advection-diffusion model within a nonlinear optimization algorithm that varied the Loihi source strength (released at the cell nearest the seamount's location) along with both the background and peak horizontal turbulent diffusivities to minimize the model mismatch to the observed distribution. We characterize the model-data misfit by computing the reduced chi-squared

$$\chi^2_\nu = \frac{1}{N-3}\sum_i \frac{(M_i - O_i)^2}{\sigma_i^2} \tag{5}$$

which is the sum of the squared differences between model (M_i) and observation (O_i) points normalized by the uncertainty (σ_i) of the observations divided by the number of constraining observations minus the number of adjustable parameters (e.g. see (Glover et al., 2011)). Since it is difficult to present the distribution of this property in three-dimensional parameter space, we present in Fig. 9 various "slices" in 2D (Fig. 9a) and 1D (Fig. 9b-d) formats along with the optimal model Loihi ^{3}He inventory spatial structure with the constraining data (Fig. 9e).

The χ^2_ν distribution as a function of source strength and maximum (peak) diffusivity is shown in Fig. 9a for a globally optimal background diffusivity of 405 m^2 s^{-1} (see Fig. 9b). The χ^2_ν contours in Fig. 9a show a sloping elliptical minimum indicating a broad correlation between source flux and diffusivity: increasing lateral diffusivity necessary to "spread" the eastward oriented tongue meridionally requires an increase in source flux required to support the overall inventory. The global minimum χ^2_ν was 1.5, indicating good agreement with observations, especially considering the simplicity of the model. The optimal case peak diffusivity was 645 m^2 s^{-1} (see Fig. 9c) and the optimal source flux (Fig. 9d) was 10.43 mol a^{-1}. The optimal source strength depends most on the aggregate horizontal diffusivity: inspection of Figs. 9b and 9d reveals that required source strength is relatively insensitive to the value of background diffusivity, changing only about ±6% for a ±50% change in background mixing rate. As one reduces the background mixing rate, the amplitude of the island wake enhancement (characterized by the sinusoid amplitude) increases to compensate, maintaining a roughly constant average diffusivity in the plume. In fact, choosing a spatially constant horizontal mixing rate has only a modest influence on the overall result.

Fig. 9e shows model ^{3}He inventory distribution for the optimal case, along with the constraining observations. The model parameters, ^{3}He source strength (10.4 mol a^{-1}) along with background (405 m^2 s^{-1}) and peak (645 m^2 s^{-1}) horizontal diffusivities scale linearly with the horizontal velocity, so assuming an uncertainty ±40% in the velocity translates to a corresponding ±40% in those parameters. Thus we estimate the ^{3}He flux to be 10.4 ± 4.2 mol a^{-1}, a peak horizontal diffusivity of 645 ± 258 m^2 s^{-1}, and a background diffusivity of 405 ± 162 m^2 s^{-1}. The range of probable horizontal diffusivities agrees well with many other estimates of intermediate depth open-ocean values on regional scales (for example, Jenkins, 1991; Ledwell et al., 1998; Robbins et al., 2000; Sundermeyer and Price, 1998). Moreover, elevated isopycnal mixing should result from the expected enhancement of deep eddy energetics around the Hawaiian Island and seamount wakes. We therefore regard the predicted fluxes and horizontal diffusivity as consistent with current understanding of those processes.

As a slab model, these calculations are relatively immune to the effects of vertical (diapycnal) mixing because the inventories used to constrain the model are vertically integrated over several hundred meters. In this way it compensates for the initial vertical dispersion caused either by enhanced vertical mixing in the vicinity of rough topography (e.g., Ledwell et al., 2000; Polzin et al., 1997) or by multiple hydrothermal injection sites at different depths. We can, nonetheless, place an upper limit on the *potential* impact of diapycnal mixing by combining our knowledge of the vertical distribution of the Loihi ^{3}He with a reasonable range of diffusivities. Estimates for open ocean deep waters are typically of the order of 1×10^{-4} m^2 s^{-1} (Munk, 1966), while tracer-based estimates in the main pycnocline are of order 2×10^{-5} m^2 s^{-1} (Ledwell et al., 1998, 1993; Rooth and Ostlund, 1972). We expect an actual diffusivity somewhere in between these two at intermediate depths. Using an average vertical ^{3}He gradient of 2×10^{-16} mol m^{-4} in the "core" of the horizontal Loihi helium plume and an approximate areal extent of 1×10^{12} m^2, we arrive at a flux of $3 - 15 \times 10^{-9}$ mol s^{-1} or 0.1 – 0.5 mol a^{-1}. This corresponds to less than 5% of the estimated flux, small compared to other uncertainties.

The most probable ^{3}He source flux of 10.4 mol a^{-1} is remarkable, being of order of 2% of the 548 ± 31 mol a^{-1} global deep hydrothermal ^{3}He flux (Bianchi et al., 2010; DeVries and Holzer, 2019; Schlitzer, 2016). While seemingly large, net plume buoyancy fluxes indicate that the Hawaiian hot spot contributes ∼15% of the global mantle plume buoyancy flux (Sleep, 1990) and since at some level in the mantle heat and ^{3}He should be correlated, a similarly large fraction of the mantle plume ^{3}He flux. Because some portion of the Hawaiian plume volatile release will be subaerial (e.g., through Kilauea, which has a ^{3}He/^{4}He ratio intermediate between Loihi and asthenospheric values), our result suggests a lower bound global plume ^{3}He flux of 70 mol a^{-1}, about 13% of the mid-ocean ridge flux (Bianchi et al., 2010; DeVries and Holzer, 2019; Schlitzer, 2016). Given an estimate of the current magma supply rate of 2.5×10^7 m^3 a^{-1} for Loihi (Garcia et al., 2006) and assuming virtually complete volatile loss, we estimate the un-degassed magmatic ^{3}He concentration of 4×10^{-7} mol m^{-3} (which corresponds to $\sim 3.5 \times 10^{-9}$ cc-STP g^{-1}). This is approximately 100-fold more than the largest reported concentrations observed in glassy rims of extruded flows on Loihi (e.g., Kurz et al., 1983), but it is consistent with the magmatic degassing concepts (e.g., Chavrit et al., 2012). Such a disparity can be expected, both due to evidence at Loihi of extensive degassing prior to eruption (Byers et al., 1985), and due to the very large ^{3}He:heat ratio observed for the Loihi hydrothermal systems (Elderfield and Schultz, 1996; Lupton et al., 1989). In the latter case, the roughly 100-fold enhancement

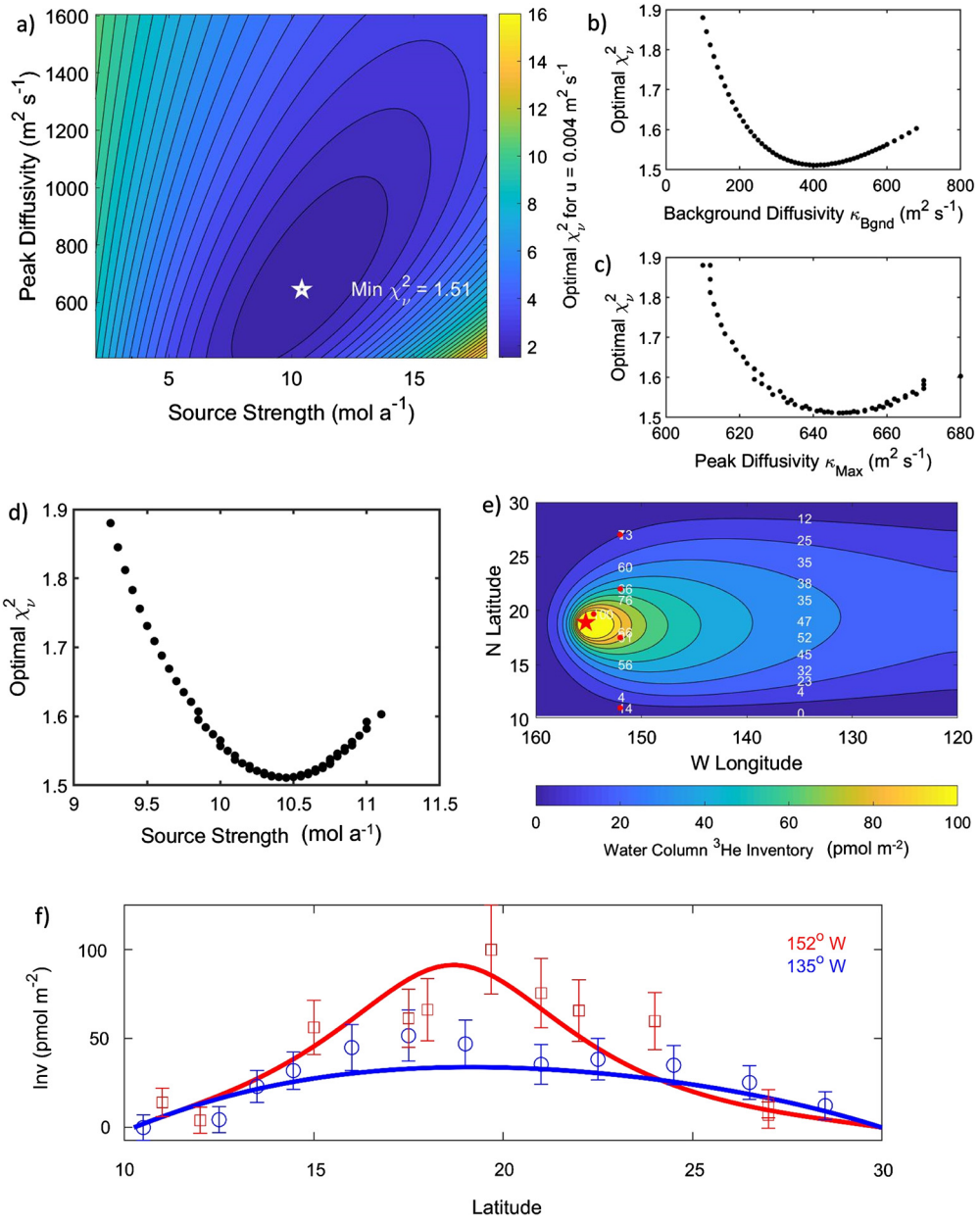

Fig. 9. **(a)** A contour plot χ^2_ν (model-data misfit) as a function of ^{3}He source strength (Loihi flux) and peak horizontal diffusivity of the case of an eastward velocity of 0.004 m s^{-1} and optimized background diffusivity of 405 m^2 s^{-1}. **(b)** The variation of optimal χ^2_ν as a function of background diffusivity, **(c)** peak diffusivity, and **(d)** source strength. **(e)** The model Loihi ^{3}He plume inventory distribution for the globally optimal case of 10.43 mol a^{-1} source strength, background diffusivity of 405 m^2 s^{-1} and 645 m^2 s^{-1} peak horizontal. Observed inventories used to constrain the optimization are posted in pmol m^{-2} (white numbers). **(f)** a comparison of measured inventories (open symbols with error bars) and optimum model prediction for the two sections (~152°W red, ~135°W blue) as a function of latitude.

of ^{3}He:heat reflects the roughly 100-fold reduction in magmatic ^{3}He concentration during ascent to the seafloor.

5. Estimating the hydrothermal iron flux

Applying the distal dFe:^{3}He ratio to this ^{3}He flux we calculate a hydrothermal iron flux of 4.3×10^7 mol a^{-1}, about 1% of the estimated ~4×10^9 mol a^{-1} global dFe flux (Resing et al., 2015). Given the relatively shallow injection depth of Loihi, this flux may be proportionately more important than implied by this low percentage. For example, an inverse analysis of oxygen and nutrient fluxes across the mid-latitude North Pacific points to significant mid-depth upwelling that peaks around 1000 – 1200 m depth (Robbins and Bryden, 1994), suggesting that this iron may reach the surface in a few decades. To evaluate the potential impact of the Loihi iron source on productivity in the North Pacific basin, we performed a numerical experiment to determine where Loihi influenced intermediate waters might reach the surface biome using the multi-tracer-optimized, global, coarse-resolution model previously developed to estimate the global hydrothermal ^{3}He flux (Schlitzer, 2016). A steady source of conservative numerical dye was released at the Loihi location on the two model depths that bracket 1100 m (983 and 1184 m) and run for 50 years. Maps of the relative amount of dye reaching the upper 100 m (as depicted by the 31 m level) are shown in Fig. 10. Both maps reveal a pronounced upwelling signature along the west coast of North America with a more subtle westward extension in the subarctic Pacific toward east coast of Kamchatka. The westward influence increases with greater release depth. This suggests that some portion of the waters that originally receive the Loihi hydrothermal iron flux must surface within the North Pacific basin within a few

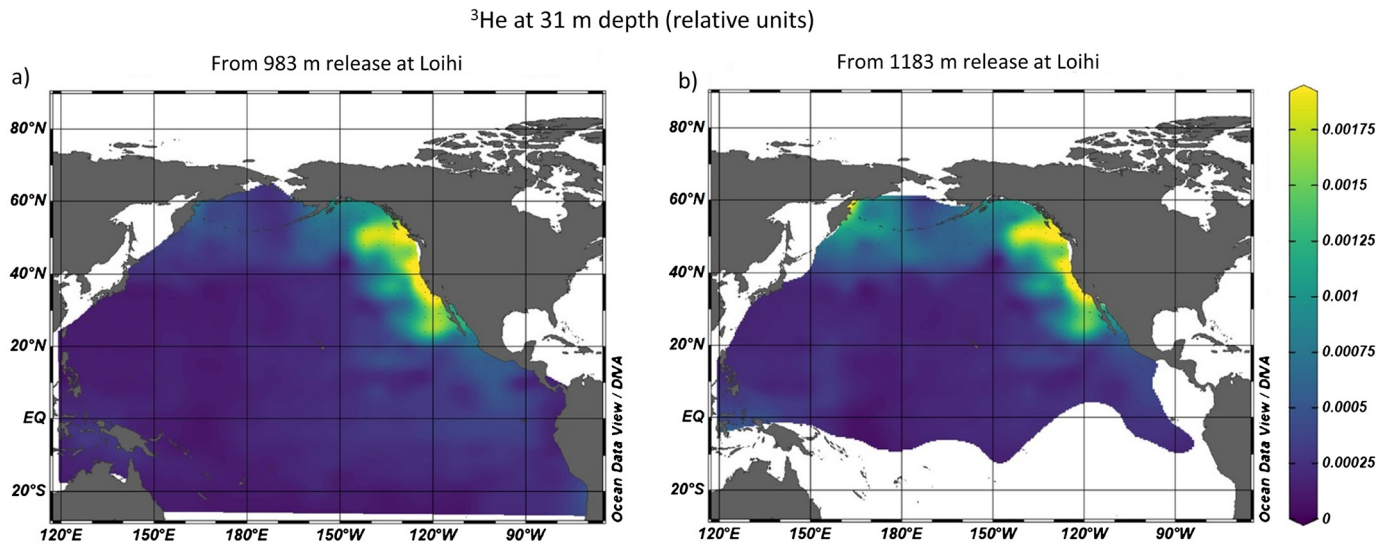

Fig. 10. Upwelling of the Loihi plume in the North Pacific in a tracer-optimized numerical model. ^{3}He concentrations (in relative units) at the model's shallowest depth (31 m) after 50 years are mapped for a tracer release from two bracketing depths: **(a)** 983 m and **(b)** 1183 m. Note the westward extension of dye for the deeper release.

decades, pointing to a potentially important role in supporting primary production for this basin (Martin and Fitzwater, 1988).

Given a range of planktonic Fe:P stoichiometries of $1-5\times10^{-3}$ (Twining and Baines, 2013) and a "Redfield" C:P ratio of 106 (Bristow et al., 2017), the Loihi Fe flux could fuel maximum basin-scale new production of $1-4\times10^{12}$ mol a^{-1} carbon. Although loss of dFe due to water column scavenging processes would reduce the Loihi hydrothermal Fe reaching surface waters (Fitzsimmons et al., 2017), we note that the deep water residence time of dFe has traditionally been thought to be longer than the 50 yr runtime of the model used in this study (70-270 years; Berquist and Boyle, 2006; Bruland et al., 1994). That is, much of the Loihi Fe may persist to be upwelled. However, shorter estimates of deep water Fe replacement timescales of $<$20 years have also been recently proposed based on comparison to Th fluxes (Hayes et al., 2018, 2015) which would suggest that perhaps none of the Loihi Fe would reach surface phytoplankton. The uncertainty in Fe scavenging rates means that the biogeochemical impact of Loihi Fe fluxes can only be assessed with a biogeochemical model containing dynamic Fe transformations. This is being pursued in a separate study. Nonetheless, it is clear that the intermediate-depth source of hydrothermal iron at Loihi has the potential to play an important role in supporting and controlling new primary production in the North Pacific Ocean.

Declaration of competing interest

The authors declare that they have no known competing financial interests or personal relationships that could have appeared to influence the work reported in this paper.

Acknowledgements

We are grateful to Bob Anderson, both for helpful comments on this manuscript and for his untiring and visionary leadership of the U.S. GEOTRACES program. This work was funded by NSF grants OCE-1756138 (helium isotopes by German, Jenkins, Lott, and Cahill), OCE-1736906 (dissolved Fe and Mn using shipboard FIA by Hatta and Weiss), OCE-1737167 (dissolved Fe and Mn using shore-based ICPMS by Fitzsimmons and Lanning), OCE-1737024 (methane by Shiller and Whitmore), OCE-1737342 (TDS and pH by Cutter and Buckley), and the overarching GP15 cruise management and logistics grants OCE-1658318 (Cutter), OCE-1657944 (Casciotti), and OCE-1657781 (Lam). This material is also based on work supported by the National Science Foundation Graduate Research Fellowship 1746932 to Lanning. We thank Zoe Sandwith, Laramie Jensen, Brent Summers, Janelle Steffen, and Virginie Sanial for their sampling and analytical work at sea, as well as the talented and dedicated sea-going technicians of the Ocean Data Facility of S.I.O. This work would not be possible without the support and cooperation of the Captain and Crew of R/V *Roger Revelle*. We also thank Robert Hamme and one anonymous reviewer for thorough and insightful comments and suggestions. All data in this publication will be made available in the next GEOTRACES data product.

References

Bennett, S.A., Hansman, R.L., Sessions, A.L., Nakamura, K.-I., Edwards, K.J., 2011. Tracing iron-fueled microbial carbon production within the hydrothermal plume at the Loihi Seamount. Geochim. Cosmochim. Acta 75, 5526–5539.

Benson, B.B., Krause Jr., D., 1980. Isotopic fractionation of helium during solution: a probe for the liquid state. J. Solution Chem. 9, 895–909.

Berger, W.H., Wefer, G., 1991. Productivity of the glacial ocean: discussion of iron hypothesis. Limnol. Oceanogr. 36, 1899–1918.

Berquist, B.A., Boyle, E.A., 2006. Dissolved iron in the tropical and subtropical Atlantic Ocean. Glob. Biogeochem. Cycles 20, GB1015.

Bianchi, D., Sarmiento, J.L., Gnanadesikan, A., Key, R.M., Schlosser, P., Newton, R., 2010. Low helium flux from the mantle inferred from simulations of oceanic helium isotope data. Earth Planet. Sci. Lett. 297, 379–386.

Bristow, L.A., Mohr, W., Ahmerkamp, S., Kuypers, M.M.M., 2017. Nutrients that limit growth in the ocean. Curr. Biol. 27, R431–R510.

Bruland, K.W., Orians, K.J., Cowen, J.P., 1994. Reactive metals in the stratified central North Pacific. Geochim. Cosmochim. Acta 58, 3171–3182.

Byers, C.D., Garcia, M.O., Muenow, D.W., 1985. Volatiles in pillow rim glasses from Loihi and Kilauea volcanoes, Hawaii. Geochim. Cosmochim. Acta 49, 1887–1896.

Carter, B.R., Radlich, J.A., Doyle, H.L., Dickson, A.G., 2013. An automated system for spectrophotometric seawater pH measurements. Limnol. Oceanogr., Methods 11, 16–27.

Charlou, J.L., Donval, J.P., Fouquet, Y., Jean-Baptiste, P., Holm, N., 2002. Geochemistry of high H_2 and CH_4 vent fluids issuing from ultramafic rocks at Rain bow hydrothermal field (36° 14'N, MAR). Chem. Geol. 191, 345–359.

Chavrit, D., Humler, E., Morizet, Y., Laporte, D., 2012. Influence of magma ascent rate on carbon dioxide degassing at oceanic ridges: message in a bubble. Earth Planet. Sci. Lett. 357–358, 376–385.

Chen, G., Wang, D., Don, C., Zu, T., Xue, H., Shu, Y., Chu, X., Qi, Y., Chen, H., 2015. Observed deep energetic eddies by seamount wake. Scientific Reports 5.

Clague, D.A., Paduan, J.B., Caress, D.W., Moyer, C.L., Glazer, B.T., Yoerger, D.R., 2019. Structure of Loihi Seamount, Hawaii, and lava flow morphology from high-resolution mapping. Front. Earth Sci. 7, 54.

Clarke, W.B., Jenkins, W.J., Top, Z., 1976. Determination of tritium by spectrometric measurement of ^{3}He. Int. J. Appl. Radiat. Isot. 27, 515–525.

Clayton, T.D., Byrne, R.H., 1993. Spectrophotometric seawater pH measurements: total hydrogen ion concentration scale calibration of m-cresol purple and at-sea results. Deep-Sea Res. 40, 2115–2129.

Cutter, G., Bruland, K.W., 2012. Rapid and noncontaminating sampling system for trace elements in global ocean surveys. Limnol. Oceanogr., Methods 10, 425–436.

DeVries, T., Holzer, M., 2019. Radiocarbon and helium isotope constraints on deep-ocean ventilation and mantle-^{3}He sources. J. Geophys. Res., Oceans 124, 3036–3057.

Duennenbier, F.K., Becker, N.C., Caplan-Auerbach, J., Clague, D.A., Cowen, J., Cremer, M., Garcia, M., Goff, F., Malahoff, A., McMurtry, G.M., Midson, B.P., Moyer, C.L., Norman, N., Okubo, P., Resing, J.A., Rhodes, J.M., Rubin, K., Sansone, F.J., Smith, J.R., Spencer, K., Wen, X., Wheat, C.G., 1997. Researchers rapidly respond to submarine activity at Loihi Volcano, Hawaii. Eos 78, 229–237.

Elderfield, H., Schultz, A., 1996. Mid-ocean ridge hydrothermal fluxes and the chemical composition of the ocean. Annu. Rev. Earth Planet. Sci. 24, 191–224.

Emerson, D., Moyer, C., 2002. Neutrophilic Fe-oxidizing bacteria are abundant at the Loihi Seamount hydrothermal vents and play a major role in Fe oxide deposition. Appl. Environ. Microbiol. 68, 3085–3093.

Emerson, D., Rentz, J.A., Lilburn, T.G., Davis, R.E., Aldrich, H., Chan, C., Moyer, C.L., 2007. A novel lineage of proteobacteria involved in formation of marine Fe-oxidizing microbial mat communities. PLoS ONE 2, e667.

Feely, R.A., Baker, E.T., Marumo, K., Urabe, T., Ishibashi, J., Gendron, J., Lebon, G.T., Okamura, K., 1996. Hydrothermal plume particles and dissolved phosphate over the superfast-spreading southern East Pacific Rise. Geochim. Cosmochim. Acta 60, 2297–2323.

Feely, R.A., Lewison, M., Massoth, G.J., Robert-Baldo, G., Lavelle, J.W., Byrne, R.H., Von Damm, K.L., Curl Jr., H.C., 1987. Composition and dissolution of black smoker particulates from active vents on the Juan de Fuca Ridge. J. Geophys. Res., Solid Earth 92, 11347–11363.

Fitzsimmons, J.N., Carrasco, G.G., Wu, J., Roshan, S., Hatta, M., Measures, C.I., Conway, T.M., John, S.G., Boyle, E.A., 2015. Partitioning of dissolved iron and iron isotopes into soluble and colloidal phases along the GA03 GEOTRACES North Atlantic Transect. Deep-Sea Res., Part 2, Top. Stud. Oceanogr. 116, 130–151.

Fitzsimmons, J.N., John, S.G., Marsay, C.M., Hoffman, C., Nicholas, S., Toner, B.M., German, C.R., Sherrell, R.M., 2017. Iron persistence in a distal hydrothermal plume supported by dissolved-particulate exchange. Nat. Geosci. 10, 195–201.

Gamo, T., Ishibashi, J., Sakai, H., Tilbrook, B., 1987. Methane anomalies in seawater above the Loihi submarine summit area, Hawaii. Geochim. Cosmochim. Acta 51, 2857–2864.

Garcia, M.O., Caplan-Auerbach, J., De Carlo, E.H., Kurz, M.D., Becker, N., 2006. Geology, geochemistry and earthquake history of Loihi Seamount, Hawaii's youngest volcano. Chem. Erde 66, 81–108.

German, C.R., Lim, D.S.S., Breier, J.A., Huber, J.A., Kobs Nawotniak, S., Shock, E., Raineault, N., 2018. Time series study of hydrothermal venting at Lo'ihi Seamount following the 2018 Kilauea eruption. Eos 14.

Glover, D.M., Jenkins, W.J., Doney, S.C., 2011. Modeling Methods for Marine Science. Cambridge University Press, Cambridge, U.K.

Hayes, C.T., Anderson, R.F., Cheng, H., Conway, T.M., Edwards, R.L., Fleisher, M.Q., Ho, P., Huang, K.-F., John, S.G., Landing, W.M., Little, S.H., Lu, Y., Morton, P.L., Moran, S.B., Robinson, L.F., Shelley, R.U., Shiller, A.M., Zheng, X.-Y., 2018. Replacement times of a spectrum of elements in the North Atlantic based on thorium supply. Glob. Biogeochem. Cycles 32, 1294–1311.

Hayes, C.T., Fitzsimmons, J.N., Boyle, E.A., McGee, D., Anderson, R.F., Weisend, R., Morton, P.L., 2015. Thorium isotopes tracing the iron cycle at the Hawaii Ocean time-series station ALOHA. Geochim. Cosmochim. Acta 169, 1–16.

Hofmann, A.W., Farnetani, C.G., Spiegelman, M., Class, C., 2011. Displaced helium and carbon in the Hawaiian plume. Earth Planet. Sci. Lett. 213, 226–236.

James, R.H., Elderfield, H., 1996. Dissolved and particulate trace metals in hydrothermal plumes at the Mid-Atlantic Ridge. Geophys. Res. Lett. 23, 3499–3502.

Jenkins, W.J., 1991. Determination of isopycnal diffusivity in the Sargasso Sea. J. Phys. Oceanogr. 21, 1058–1061.

Jenkins, W.J., Doney, S.C., Fendrock, M., Fine, R.A., Gamo, T., Jean-Baptiste, P., Key, R., Klein, B., Lupton, J.E., Newton, R., Rhein, M., Roether, W., Sano, Y., Schlitzer, R., Schlosser, P., Swift, J.H., 2019a. A comprehensive global oceanic dataset of helium isotope and tritium measurements. Earth Syst. Sci. Data 11, 441–454.

Jenkins, W.J., Lott III, D.E., Cahill, K.L., 2019b. A determination of atmospheric helium, neon, argon, krypton, and xenon solubility concentrations in water and seawater. Mar. Chem. 211, 94–107.

Jenkins, W.J., Lott III, D.E., German, C.R., Cahill, K.L., Goudreau, J., Longworth, B.E., 2018. The deep distributions of helium isotopes, radiocarbon, and noble gases along the U.S. GEOTRACES East Pacific zonal transect (GP16). Mar. Chem. 201, 167–182.

Jenkins, W.J., Lott III, D.E., Longworth, B.E., Curtice, J.M., Cahill, K.L., 2015. The distributions of helium isotopes and tritium along the U.S. GEOTRACES North Atlantic sections (GEOTRACES GA03). Deep-Sea Res., Part 2, Top. Stud. Oceanogr. 116, 21–28.

Jensen, L.T., Wyatte, N.J., Landing, W.J., Fitzsimmons, J.N., 2020. Assessment of the stability, sorption, and exchangeability of marine dissolved and colloidal metal. Mar. Chem. 220. https://doi.org/10.1016/j.marchem.2020.103754.

Johnson, K.S., Coale, K.H., Berelson, W.M., Gordon, R.M., 1996. On the formation of the manganese maximum in the oxygen minimum. Geochim. Cosmochim. Acta 60, 1291–1299.

Kaneoka, I., Takaoka, N., Clague, D., 1983. Noble gas systematics for coexisting glass and olivine crystals in basalts and dunite xenoliths from Loihi Seamount. Earth Planet. Sci. Lett. 66, 427–437.

Keir, R.S., 2010. A note on the fluxes of abiogenic methane and hydrogen from mid-ocean ridges. Geophys. Res. Lett. 37.

Kurz, M.D., Jenkins, W.J., Hart, S.R., 1982. Helium isotopic systematics of oceanic islands and mantle heterogeneity. Nature 297, 43–47.

Kurz, M.D., Jenkins, W.J., Hart, S.R., Clague, D., 1983. Helium isotopic variations in volcanic rocks from Loihi Seamount and the islands of Hawaii. Earth Planet. Sci. Lett. 66, 388–406.

Lagerstrom, M.E., Field, M.P., Seguret, M., Fischer, L., Hann, S., Sherrell, R.M., 2013. Automated on-line flow-injected ICP-MS determination of tracer metals (Mn, Fe, Co, Ni, Cu, and Zn) in open ocean seawater: application to GEOTRACES program. Mar. Chem. 155, 71–80.

Ledwell, J.R., Montgomery, E.T., Polzin, K.L., St. Laurent, L.C., Schmitt, R.W., Toole, J.M., 2000. Evidence for enhanced mixing over rough topography in the abyssal ocean. Nature 403, 179–182.

Ledwell, J.R., Watson, A., Law, C.S., 1998. Mixing of a tracer in the pycnocline. J. Geophys. Res. 103, 21499–21529.

Ledwell, J.R., Watson, A.J., Law, C.S., 1993. Evidence for slow mixing rates across the pycnocline from an open-ocean tracer-release experiment. Nature 364, 701–703.

Lueck, R.G., Mudge, T.D., 1997. Topographically induced mixing around a shallow seamount. Science 276, 1831–1833.

Lupton, J.E., 1996. A far-field hydrothermal plume from Loihi Seamount. Science 272, 976–979.

Lupton, J.E., 1998. Hydrothermal helium plumes in the Pacific Ocean. J. Geophys. Res. 103, 15853–15868.

Lupton, J.E., Baker, E.T., Massoth, G.J., 1989. Variable 3He/heat ratios in submarine hydrothermal systems: evidence from two plumes over the Juan de Fuca ridge. Nature 337, 161–164.

Martin, J.H., Fitzwater, S.E., 1988. Iron deficiency limits phytoplankton growth in the north-east Pacific subarctic. Nature 331, 341–343.

Martin, J.H., Gordon, R.M., 1988. Northeast Pacific iron distributions in relation to phytoplankton productivity. Deep-Sea Res., Part 1, Oceanogr. Res. Pap. 35, 177–196.

Measures, C.I., Yang, J., Resing, J.A., 1995. Determination of iron in seawater by flow injection analysis using in-line preconcentration and spectrophotometric detection. Mar. Chem. 50, 3–12.

Munk, W.H., 1966. Abyssal recipes. Deep-Sea Res. 13, 707–730.

Ollitrault, M., De Verdiere, A.C., 2014. The ocean general circulation near 1000-m depth. J. Phys. Oceanogr. 44, 384–409.

Polzin, K.L., Toole, J.M., Ledwell, J.R., Schmitt, R.W., 1997. Spatial variability of turbulent mixing in the abyssal ocean. Science 276, 93–96.

Radford-Knoery, J., Cutter, G.A., 1993. Determination of carbonyl sulfide and hydrogen sulfide species in natural waters using specialized collection procedures and gas chromatography with flame detection. Anal. Chem. 65, 976–982.

Resing, J.A., Mottl, M.J., 1992. Determination of manganese in seawater using flow injection analysis with on-line preconcentration and spectrophotometric detection. Anal. Chem. 64, 2682–2687.

Resing, J.A., Sedwick, P.N., German, C.R., Jenkins, W.J., Moffett, J.W., Sohst, B.M., Tagliabue, A., 2015. Basin-scale transport of hydrothermal dissolved metals across the South Pacific Ocean. Nature 523, 203–206.

Rison, W., Craig, H., 1983. Helium isotopes and mantle volatiles in Loihi Seamount and Hawaiian Island basalts and xenoliths. Earth Planet. Sci. Lett. 66, 407–426.

Robbins, P.E., Bryden, H.L., 1994. Direct observations of advective nutrient and oxygen fluxes at 24°N in the Pacific Ocean. Deep-Sea Res. 41, 143–168.

Robbins, P.E., Price, J.F., Owens, W.B., Jenkins, W.J., 2000. On the importance of lateral diffusion for the ventilation of the lower thermocline in the subtropical North Atlantic. J. Phys. Oceanogr. 30, 67–89.

Roberts, H.M., Shiller, A.M., 2015. Determination of dissolved methane in natural waters using headspace analysis with cavity ringdown spectroscopy. Anal. Chim. Acta 856, 68–73.

Rooth, C.G., Ostlund, H.G., 1972. Penetration of tritium into the North Atlantic thermocline. Deep-Sea Res. 19, 481–492.

Rouxel, O., Toner, B., Germain, Y., Glazer, B., 2018. Geochemical and iron isotopic insights into hydrothermal iron deposit formation at Loihi Seamount. Geochim. Cosmochim. Acta 220, 449–482.

Saito, M.A., Noble, A.E., Tagliabue, A., Goepfert, T.J., Lamborg, C.H., Jenkins, W.J., 2013. Slow-spreading submarine ridges in the South Atlantic as a significant oceanic iron source. Nat. Geosci. 6, 775–779.

Schlitzer, R., 2004. Export production in the Equatorial and North Pacific derived from dissolved oxygen, nutrient and carbon data. J. Oceanogr. 60, 53–62.

Schlitzer, R., 2007. Assimilation of radiocarbon and chlorofluorocarbon data to constrain deep and bottom water transports in the world ocean. J. Phys. Oceanogr. 37, 259–276.

Schlitzer, R., 2016. Quantifying He fluxes from the mantle using multi-tracer data assimilation. Philos. Trans. R. Soc. A 374. https://doi.org/10.1098/rsta.2015.0288.

Schlitzer, R., Anderson, R.F., Dodas, E.M., Lohan, M., Geibert, W., Tagliabue, A., Bowie, A., Jeandel, C., Maldonado, M.T., Landing, W.M., Cockwell, D., Abadie, C., Abouchami, W., Achterberg, E.P., Agather, A., Aguliar-Islas, A., van Aken, H.M., Andersen, M., Archer, C., Auro, M., de Baar, H.J., Baars, O., Baker, A.R., Bakker, K., Basak, C., Baskaran, M., Bates, N.R., Bauch, D., van Beek, P., Behrens, M.K., Black, E., Bluhm, K., Bopp, L., Bouman, H., Bowman, K., Bown, J., Boyd, P., Boye, M., Boyle, E.A., Branellec, P., Bridgestock, L., Brissebrat, G., Browning, T., Bruland, K.W., Brumsack, H.-J., Brzezinski, M., Buck, C.S., Buck, K.N., Buesseler, K., Bull, A., Butler, E., Cai, P., Mor, P.C., Cardinal, D., Carlson, C., Carrasco, G., Casacuberta, N., Casciotti, K.L., Castrillejo, M., Chamizo, E., Chance, R., Charette, M.A., Chaves, J.E., Cheng, H., Chever, F., Christl, M., Church, T.M., Closset, I., Colman, A., Conway, T.M., Cossa, D., Croot, P., Cullen, J.T., Cutter, G.A., Daniels, C., Dehairs, F., Deng, F., Dieu, H.T., Duggan, B., Dulaquais, G., Dumousseaud, C., Echegoyen-Sanz, Y., Edwards, R.L., Ellwood, M., Fahrbach, E., Fitzsimmons, J.N., Russell Flegal, A., Fleisher, M.Q., van de Flierdt, T., Frank, M., Friedrich, J., Fripiat, F., Fröllje, H., Galer, S.J.G., Gamo, T., Ganeshram, R.S., Garcia-Orellana, J., Garcia-Solsona, E., Gault-Ringold, M., George, E., Gerringa, L.J.A., Gilbert, M., Godoy, J.M., Goldstein, S.L., Gonzalez, S.R., Grissom, K., Hammerschmidt, C., Hartman, A., Hassler, C.S., Hathorne, E.C., Hatta, M., Hawco, N., Hayes, C.T., Heimbürger, L.-E., Helgoe, J., Heller, M., Henderson, G.M., Henderson, P.B., van Heuven, S., Ho, P., Horner, T.J., Hsieh, Y.-T., Huang, K.-F., Humphreys, M.P., Isshiki, K., Jacquot, J.E., Janssen, D.J., Jenkins, W.J., John, S., Jones, E.M., Jones, J.L., Kadko, D.C., Kayser, R., Kenna, T.C., Khondoker, R., Kim, T., Kipp, L., Klar, J.K., Klunder, M., Kretschmer, S., Kumamoto, Y., Laan, P., Labatut, M., Lacan, F., Lam, P.J., Lambelet, M., Lamborg, C.H., Le Moigne, F.A.C., Le Roy, E., Lechtenfeld, O.J., Lee, J.-M., Lherminier, P., Little, S., López-Lora, M., Lu, Y., Masque, P., Mawji, E., McClain, C.R., Measures, C., Mehic, S., Barraqueta, J.-L.M., van der Merwe, P., Middag, R., Mieruch, S., Milne, A., Minami, T., Moffett, J.W., Moncoiffe, G., Moore, W.S., Morris, P.J., Morton, P.L., Nakaguchi, Y., Nakayama, N., Niedermiller, J., Nishioka, J., Nishiuchi, A., Noble, A., Obata, H., Ober, S., Ohnemus, D.C., van Ooijen, J., O'Sullivan, J., Owens, S., Pahnke, K., Paul, M., Pavia, F., Pena, L.D., Peters, B., Planchon, F., Planquette, H., Pradoux, C., Puigcorbé, V., Quay, P., Queroue, F., Radic, A., Rauschenberg, S., Rehkämper, M., Rember, R., Remenyi, T., Resing, J.A., Rickli, J., Rigaud, S., Rijkenberg, M.J.A., Rintoul, S., Robinson, L.F., Roca-Martí, M., Rodellas, V., Roeske, T., Rolison, J.M., Rosenberg, M., Roshan, S., Rutgers van der Loeff, M.M., Ryabenko, E., Saito, M.A., Salt, L.A., Sanial, V., Sarthou, G., Schallenberg, C., Schauer, U., Scher, H., Schlosser, C., Schnetger, B., Scott, P., Sedwick, P.N., Semiletov, I., Shelley, R., Sherrell, R.M., Shiller, A.M., Sigman, D.M., Singh, S.K., Slagter, H.A., Slater, E., Smethie, W.M., Snaith, H., Sohrin, Y., Sohst, B., Sonke, J.E., Speich, S., Steinfeldt, R., Stewart, G., Stichel, T., Stirling, C.H., Stutsman, J., Swarr, G.J., Swift, J.H., Thomas, A., Thorne, K., Till, C.P., Till, R., Townsend, A.T., Townsend, E., Tuerena, R., Twining, B.S., Vance, D., Velazquez, S., Venchiarutti, C., Villa-Alfageme, M., Vivancos, S.M., Voelker, A.H.L., Wake, B., Warner, M.J., Watson, R., van Weerlee, E., Alexandra Weigand, M., Weinstein, Y., Weiss, D., Wisotzki, A., Woodward, E.M.S., Wu, J., Wu, Y., Wuttig, K., Wyatt, N., Xiang, Y., Xie, R.C., Xue, Z., Yoshikawa, H., Zhang, J., Zhang, P., Zhao, Y., Zheng, L., Zheng, X.-Y., Zieringer, M., Zimmer, L.A., Ziveri, P., Zunino, P., Zurbrick, C. (Eds.), 2018. The GEOTRACES intermediate data product. Chem. Geol. 493, 2017 210–223.

Sedwick, P.N., McMurtry, G.M., Macdougall, J.D., 1992. Chemistry of hydrothermal solutions from Pele's Vents, Loihi Seamount, Hawaii. Geochim. Cosmochim. Acta 56, 3643–3667.

Sleep, N.H., 1990. Hotspots and mantle plumes: some phenomenology. J. Geophys. Res., Solid Earth 95, 6715–6736.

Stanley, R.H.R., Baschek, B., Lott III, D.E., Jenkins, W.J., 2009. A new automated method for measuring noble gases and their isotopic ratios in water samples. Geochem. Geophys. Geosyst. 10, Q05008. https://doi.org/10.1029/2009GC002429.

Sundermeyer, M.A., Price, J.F., 1998. Lateral mixing and the North Atlantic Tracer Release Experiment: observations and numerical simulations of Lagrangian particles and a passive tracer. J. Geophys. Res. 103, 21481–21497.

Tagliabue, A., Bopp, L., Dutay, J.-C., Bowie, A.R., Chever, F., Jean-Baptiste, P., Bucciarelli, E., Lannuzel, D., Remenyi, T., Sarthou, G., Aumont, O., Gehlen, M., Jeandel, C., 2010. Hydrothermal contribution to the oceanic dissolved iron inventory. Nat. Geosci. 3, 252–256.

Tagliabue, A., Bowie, A.R., Boyd, P.W., Buck, K.N., Johnson, K.S., Saito, M.A., 2017. The integral role of iron in ocean biogeochemistry. Nature 543, 51–59.

Toole, J.M., Schmitt, R.W., Polzin, K.L., Kunze, E., 1997. Near-boundary mixing above the flanks of a midlatitude seamount. J. Geophys. Res., Oceans 102, 947–959.

Twining, B.S., Baines, S.B., 2013. The trace metal composition of marine phytoplankton. Annu. Rev. Mar. Sci. 5, 191–215.

Von Damm, K., 1985. Controls on the chemistry and temporal variability of seafloor hydrothermal fluids. In: Humphris, S.E., Zierenberg, R.A., Mullineaux, L.S., Thomson, R.E. (Eds.), Seafloor Hydrothermal Systems: Physical, Chemical, Biological, and Geological Interactions. AGU, Washington, D.C., pp. 222–247.

Von Damm, K.L., Lilley, M.D., Shanks III, W.C., Brockington, M., Bray, A.M., O'Grady, K.M., Olson, E., Graham, A., Proskurowski, G., Party, t S.S., 2003. Extraordinary phase separation and segregation in vent fluids from the southern East Pacific Rise. Earth Planet. Sci. Lett. 206, 365–378.

Wang, D.T., Reeves, E.P., McDermott, J.M., Seewald, J.S., Ono, S., 2018. Clumped isotopologue constraints on the origin of methane at seafloor hot springs. Geochim. Cosmochim. Acta 223, 141–158.

Young, C., Lupton, J.E., 1983. An ultratight fluid sampling system using cold-welded copper tubing. Eos 64, 735.